

# Northumbria Research Link

Citation: Talakokula, V., Bhalla, S., Ball, Richard, Bowen, Chris, Pesce, Giovanni, Kurchania, R., Bhattacharjee, B., Gupta, A. and Paine, Kevin (2016) Diagnosis of carbonation induced corrosion initiation and progression in reinforced concrete structures using piezo-impedance transducers. *Sensors and Actuators A: Physical*, 242. pp. 79-91. ISSN 0924-4247

Published by: Elsevier

URL: <http://dx.doi.org/10.1016/j.sna.2016.02.033>  
<<http://dx.doi.org/10.1016/j.sna.2016.02.033>>

This version was downloaded from Northumbria Research Link:  
<http://nrl.northumbria.ac.uk/id/eprint/27338/>

Northumbria University has developed Northumbria Research Link (NRL) to enable users to access the University's research output. Copyright © and moral rights for items on NRL are retained by the individual author(s) and/or other copyright owners. Single copies of full items can be reproduced, displayed or performed, and given to third parties in any format or medium for personal research or study, educational, or not-for-profit purposes without prior permission or charge, provided the authors, title and full bibliographic details are given, as well as a hyperlink and/or URL to the original metadata page. The content must not be changed in any way. Full items must not be sold commercially in any format or medium without formal permission of the copyright holder. The full policy is available online: <http://nrl.northumbria.ac.uk/policies.html>

This document may differ from the final, published version of the research and has been made available online in accordance with publisher policies. To read and/or cite from the published version of the research, please visit the publisher's website (a subscription may be required.)

# Diagnosis of carbonation induced corrosion initiation and progression in reinforced concrete structures using piezo-impedance transducers

*V. Talakokula<sup>1</sup>, S. Bhalla<sup>2\*</sup>, R. J. Ball<sup>3</sup>, C. R. Bowen<sup>4</sup>, G. L. Pesce<sup>3</sup>, R. Kurchania<sup>5</sup>, B. Bhattacharjee<sup>2</sup>, A. Gupta<sup>2</sup>, and K. Paine<sup>3</sup>*

## ABSTRACT

In addition to chloride induced corrosion, the other commonly occurring type of rebar corrosion in reinforced concrete structures is that induced by the ingress of atmospheric carbon dioxide into concrete, commonly referred to as ‘carbonation induced corrosion’. This paper presents a new approach for detecting the onset and quantifying the level of carbonation induced rebar corrosion. The approach is based on the changes in the mechanical impedance parameters acquired using the electro-mechanical coupling of a piezoelectric lead zirconate titanate (PZT) ceramic patch bonded to the surface of the rebar. The approach is non-destructive and is demonstrated through accelerated tests on reinforced concrete specimens subjected to controlled carbon dioxide exposure for a period spanning over 230 days. The equivalent stiffness parameter, extracted from the frequency response of the admittance signatures of the PZT patch, is found to increase with penetration of carbon dioxide inside the surface and the consequent carbonation, an observation that is correlated with phenolphthalein staining. After the onset of rebar corrosion, the equivalent stiffness parameter exhibited a reduction in magnitude over time, providing a clear indication of the occurrence of corrosion and the results are correlated with scanning electron microscope images and Raman spectroscopy measurements. The average rate of corrosion is determined using the equivalent mass parameter. The use of PZT ceramic transducers, therefore, provides an alternate and effective technique for diagnosis of carbonation induced rebar corrosion initiation and progression in reinforced concrete structures non-destructively.

**Key words:** SEM, Chloride, Corrosion, Carbonation, Steel Reinforced concrete

---

<sup>1</sup>Department of Civil Engineering, ABES Engineering College, Ghaziabad, (INDIA).

<sup>2</sup>Department of Civil Engineering, Indian Institute of Technology Delhi, Hauz Khas, New Delhi 110016 (INDIA).

<sup>3</sup>Department of Architecture and Civil Engineering, University of Bath, Bath, BA2 7AY, (UNITED KINGDOM)

<sup>4</sup>Department of Mechanical Engineering, University of Bath, Bath, BA2 7AY, (UNITED KINGDOM)

<sup>5</sup>Department of Physics, Maulana Azad National Institute of Technology (MANIT), Bhopal, 462051 (INDIA)

\*Corresponding author (Email: [sbhalla@civil.iitd.ac.in](mailto:sbhalla@civil.iitd.ac.in))

## 1. INTRODUCTION

Rebar corrosion is widely regarded as the most common cause of deterioration and premature failure of reinforced concrete (RC) structures [1]. In general, concrete is expected to provide a high degree of corrosion protection to the embedded steel rebars owing to its highly alkaline nature. A well compacted and cured concrete, with low water-cement ratio, has a permeability that is low enough to inhibit the penetration of corrosion inducing agents from the environment. However, such ideal conditions are seldom met in practice, leading to corrosion of the reinforcement, which is the major tensile load resisting element in RC structures.

Rebar corrosion is of two types, namely (i) chloride induced and (ii) carbonation induced. In the first type, chloride ions, either present in the raw materials or introduced from outside, due to insufficient cover or high permeability, lead to a breakdown of the alkaline passive film around the rebar [2, 3]. The second type of rebar corrosion, namely carbonation induced corrosion, results from the ingress of atmospheric carbon dioxide ( $\text{CO}_2$ ) into the concrete. The penetrated  $\text{CO}_2$  dissolves in the pore solution to form carbonic acid, which reacts with calcium hydroxide and unhydrated silicates in the cement paste, forming mainly calcium carbonate [4]. Although calcium carbonate fills up the concrete pores leading to a somewhat lower permeability, the associated drop in the pore fluid alkalinity from a pH value of over 12 to as low as 8 disrupts the passivating layer surrounding the steel reinforcement, leading to corrosion [5]. Irrespective of whether the primary mechanism is chloride or carbonation induced, rebar corrosion is generally accompanied by the loss of cross section and the accumulation of corrosion products, which occupy much larger volume than the original steel. Hence, this process generates tensile stresses, which leads to cracking

and spalling of the concrete [3]. Rebar corrosion may not necessarily imply structural collapse but it causes significant loss of structural serviceability.

A wide range of electro-chemical/non electro-chemical techniques and sensors based techniques have been reported in the literature for the purpose of diagnosing and quantification of the rebar corrosion. Table 1 summarises some of the techniques along with their advantages and limitations [6]. Recently Miller [7] had described an inductive sensor used to image steel reinforcement bars in concrete and visualise surface corrosion. The present research uses the electro-mechanical impedance (EMI) technique which has recently emerged as a promising tool for structural health monitoring (SHM) and non-destructive evaluation (NDE) for a wide variety of materials and structures. This technique works by comparing the sensor response in a healthy (undamaged) structure to the response measured at a specific time point of interest. Differences are then associated with chemical change, such as corrosion, or a physical change such as cracking.

Talakokula et. al [6] recently proposed an EMI based approach for detecting and measuring the level of chloride induced rebar corrosion, validated through accelerated corrosion tests on embedded rebars. This paper focuses on extending the approach to carbonation induced corrosion, which operates with a somewhat different mechanism and report on studies involving accelerated carbonation tests carried out on cylindrical specimens, spanning over 230 days of exposure. The corrosion assessment is based on the mechanical impedance parameters determined from EMI signatures of a piezoelectric lead zirconate titanate (PZT) ceramic patch bonded to the surface of the rebar. The PZT based equivalent stiffness parameter (ESP) and equivalent mass parameter (EMP) has been primarily employed for corrosion assessment. The results

are correlated with phenolphthalein stain test and high resolution microscopic images. The following sections of the paper cover the physical principles of the EMI technique followed by experimental results and analysis.

## 2. FUNDAMENTALS OF THE ELETRO-MECHANICAL IMPEDANCE (EMI) TECHNIQUE

Piezoelectric materials are categorized as ‘smart’ materials owing to their ‘stimulus-response’ behaviour, exhibited with reference to mechanical and electrical domains. When subjected to mechanical stresses, a PZT patch develops surface charges, a phenomenon called the ‘direct piezoelectric effect’. Similarly, when subjected to an electric field, it undergoes mechanical strain, often referred to as the ‘converse piezoelectric effect’. The direct and the converse effects are mathematically represented by Eqs. (1) and (2) respectively [8]:

$$D_3 = \overline{\varepsilon_{33}^T} E_3 + d_{31} T_1 \quad (1)$$

$$S_1 = \frac{T_1}{\overline{Y^E}} + d_{31} E_3 \quad (2)$$

where  $S_1$  is the strain along axis ‘1’,  $D_3$  the electric displacement over the surface of the PZT patch,  $d_{31}$  the piezoelectric strain coefficient and  $T_1$  the axial stress in the patch along axis ‘1’. It is assumed that the axis ‘3’ points along the thickness of the PZT patch and the axes ‘1’ and ‘2’ lie in the plane of the patch as shown in Fig. 1 (a) and (b) for a typical PZT patch.  $\overline{Y^E} = Y^E (1 + \eta j)$  represents the Young’s modulus of the patch at constant electric field and  $\overline{\varepsilon_{33}^T} = \varepsilon_{33}^T (1 - \delta j)$  is its electric permittivity at constant stress, with  $\eta$  and  $\delta$  denoting the mechanical loss factor and the dielectric loss factor respectively.

The EMI technique, which is the tool used in this paper for diagnosing the corrosion initiation and progression, exploits the direct and the converse effects simultaneously and has been demonstrated to be capable for SHM of a wide variety of engineering structures, ranging from laboratory sized components to large prototype structures [9-12]. Several new cost-effective variants of the technique have also been proposed [13-15]. The EMI technique is essentially vibration based in nature, however operating in a somewhat high frequency range of 30-400 kHz. Such high frequencies of vibrations are achieved by electrically exciting the PZT patch (in turn bonded to the surface of the structure to be monitored), by means of an impedance analyzer/ inductance capacitance and resistance (LCR) meter. Under such external field excitation, the bonded patch induces deformations in the host structure (converse effect), whose response is transferred back to the patch (direct effect) in the form of an admittance signature, consisting of the conductance ' $G$ ' (real part) and the susceptance ' $B$ ' (imaginary part). Frequencies in excess of 500 kHz are not favourable due to a strong possibility of the sensing region becoming extremely localized relative to the PZT patch [7, 16]. It is of interest to note that in this context, the conductance/ susceptance relate to the piezoceramic sensor and its electro-mechanical response due to the mechanical properties of its surrounding environment; it is therefore not possible to specifically relate the sensor conductance to that of the galvanic corrosion process on the surface of the rebar. Any damage to the host structure affects the dual process (direct and converse effect) and leads to a change in the admittance spectrum, that is, the plot of conductance/susceptance as a function of frequency. This in turn provides the necessary Indication for detection of damage. Liang et. al [17] proposed the impedance based analytical formulations to model PZT-structure electro-mechanical interaction in 1D structures that are relevant to the EMI technique. Bhalla and Soh [18] extended Liang's

impedance formulations to 2D structures, (Fig. 1c), by introducing the concept of ‘effective impedance’. They had taken into account the signatures of the PZT patch prior to integration into the structure, often termed ‘free-free’. Use of these signatures in the governing 2D wave equation, allowed derivation of the following expression for the complex electro-mechanical admittance  $\bar{Y}$  as

$$\bar{Y} = G + Bj = 4\omega j \frac{l^2}{h} \left[ \frac{\bar{\epsilon}_{33}^T}{\epsilon_{33}^T} - \frac{2d_{31}^2 \bar{Y}^E}{(1-\nu)} + \frac{2d_{31}^2 \bar{Y}^E}{(1-\nu)} \left( \frac{Z_{a,eff}}{Z_{s,eff} + Z_{a,eff}} \right) \bar{T} \right] \quad (3)$$

where,  $l$  is the half-length of the patch,  $\nu$  the Poisson’s ratio of the patch and  $\omega$  the angular frequency. The term  $\bar{T}$  is the complex tangent ratio, ideally equal to  $\tan(kl)/kl$ , with  $k = \omega \sqrt{\rho(1-\nu^2) / \bar{Y}^E}$  being the wave number. Correction factors  $C_1$  and  $C_2$  (determined from the signatures of the PZT patch in the ‘free-free’ condition) were introduced by Bhalla and Soh [18] to realistically represent the behaviour of an actual PZT patch, introducing the modifying expression for  $\bar{T}$  as

$$\bar{T} = \frac{1}{2} \left( \frac{\tan(C_1 kl)}{C_1 kl} + \frac{\tan(C_2 kl)}{C_2 kl} \right) \quad (4)$$

Further, the modified mechanical impedance of the PZT patch was derived as

$$Z_{a,eff} = \frac{2h \bar{Y}^E}{j\omega(1-\nu)\bar{T}} \quad (5)$$

It can be observed from Eq. (3) that any damage to the host structure (i.e. any change in mechanical impedance ‘ $Z_{s,eff}$ ’) will induce a deviation in  $\bar{Y}$ , thereby providing an indication of the damage. Using the computational procedure outlined by Bhalla and Soh [19], Eq. (3) can be utilized to obtain the real and the imaginary components ( $x$  and  $y$  respectively) of the structural impedance  $Z_{s,eff} = x + yj$  at a particular angular

frequency  $\omega$  from the measured  $G$  and  $B$  values. Thus, bonding a PZT patch to a structure and measuring its admittance signature enables the determination of the drive point mechanical impedance of the structure,  $Z_{s,eff} = x + yj$ , from the measured data alone, without demanding any *a priori* information governing the phenomenological nature of the structure. Depending upon the variation of ‘ $x$ ’ and ‘ $y$ ’ with frequency and the associated values, the inherent elements constituting the host structure can be identified [20]. Soh and Bhalla [11] and Bhalla et. al [12] found in their experiments that the PZT patches identified the host structure as a *Kelvin-Voigt* system, consisting of a parallel combination of spring and the damper elements. The stiffness element, termed as the ESP, has been found to be related to the actual stiffness of the host structure. Monitoring the ESP at different times provides an accurate condition of the residual stiffness of the structure and can be employed for SHM.

The next sections describe the identification of structural system based on the values of ‘ $x$ ’ and ‘ $y$ ’ and utilization of the ESP for monitoring and quantifying the severity of the structural damage induced by carbonation on rebars embedded in concrete.

### **3. ACCELERATED CARBONATION TESTS ON RC SPECIMENS:**

#### **EXPERIMENTAL PROCEDURE**

Four RC cylinders of grade M30 [21] were cast with diameters of 25, 35, 45 and 60 mm respectively and length 100 mm, as described in Table 2. A single piece of 16 mm diameter high yield deformed (HYD) steel rebar, grade Fe415 [22], was cast at the centre of each cylinder. The rebar’s length was 130 mm, allowing 30 mm to project out at one end of the cylinder, as shown in Fig. 2. The four different diameters provided concrete cover depths of 4.5, 9.5, 14.5 and 22 mm respectively. Specimen number 1, with a cover depth 22 mm, was employed as a reference for the purpose of monitoring

carbonation penetration depth through phenolphthalein staining. No PZT patch was attached to the reference sample as this was to be used for destructive testing such as for phenolphthalein test measurements to determine the carbonation depth and imaging analysis. On the other samples, a PZT patch measuring 10×10×0.3 mm (Fig. 1a), of ferroelectric grade PIC 151 [23] was bonded to each rebar at the mid length, where a small flat surface was achieved through machining to allow for the bonding of the patch, as shown in Fig. 2. A thin layer of epoxy was applied on the machined rebar surface first and the PZT patch was placed on it; the whole set-up was then kept undisturbed at room temperature for 24 h to enable full curing of the adhesive, after which wires were soldered to the PZT patch's electrodes. The PZT patch was then covered with an additional thin layer of epoxy adhesive as a protective measure. The concrete cylindrical specimens were cast using ordinary Portland cement (OPC) 53 Grade, fine aggregate of Zone 1 grading [24] and crushed coarse aggregate of nominal size 10 mm. Table 3 presents the details of the composition of the concrete mix. The moulds were filled with concrete in three layers along with the rebar (with the PZT patch bonded on it), taking particular care in pouring the concrete to avoid damage to the sensor. The concrete was compacted carefully using a table vibrator. For the 25 mm diameter specimen, it was necessary to remove some of the larger pieces of the aggregate from the mortar at the time of casting to accommodate the thin concrete cover of 4.5 mm. The specimens were demoulded after 24 h of casting. The soldered electrodes of the PZT patch were connected to an LCR meter (Agilent E4980 [25]). In this manner, the electro mechanical admittance signature, consisting of the real part ( $G$ ) and the imaginary part ( $B$ ) were acquired in the frequency range of 50-400 kHz. A frequency interval of 100 Hz was used for each impedance measurement.

Compared to chloride-induced corrosion, carbonation is a slower process. In high-quality concrete, it has been estimated that carbonation will proceed at a rate of not more than 1.0 mm per year [26]. The carbonation rate is significantly increased in concrete with a high water-cement ratio (more than specified by IS 10262, 2009 [27]), low cement content, short curing period, lower strength, and highly permeable or porous paste. In addition, the carbonation rate is highly dependent on the relative humidity of the concrete. The highest rates of carbonation occur when the relative humidity ranges between 50 % and 75 %. Carbonation-induced corrosion typically occurs on areas of building facades that are exposed to rainfall, shaded from sunlight, and have smaller concrete cover over the reinforcing steel [27]. Since the carbonation process is too slow under natural conditions, accelerated carbonation is preferred in the laboratory investigations since the 1960's [28]. In the present study, the accelerated corrosion experiments were initiated after a period of 28 days from the day of casting, assuming that any further concrete strength gain on account of concrete curing is negligible.

After the baseline signatures were acquired, the specimens were placed in a carbonation chamber. The CO<sub>2</sub> concentration in the chamber was maintained at 5 % under a relative humidity of 75±5 % and temperature of 25°C. Studies of the chemical changes and phase analysis of Portland cement pastes under conditions of accelerated carbonation in excess of 3 % (CO<sub>2</sub> concentration) have been conducted by Castellote and colleagues [29]. They demonstrated that, where CO<sub>2</sub> concentrations were in excess of 3 %, microstructural changes were observed compared to ambient conditions. This should be considered when translating results from this study to systems carbonating under ambient conditions. Wax was applied to the circular ends of each cylindrical samples to allow CO<sub>2</sub> ingress radially from the sides only. During the accelerated carbonation

exposure, the admittance signatures were acquired at frequent intervals throughout the experimental exposure period of 230 days. In order to measure the carbonation penetration depth, a 50 mm thick slice was cut from the bottom of the reference specimen, as shown in Fig. 4 and the fracture surface was sprayed with a saturated solution of phenolphthalein indicator in ethanol. The slicing was done on the same face in dry conditions. However, the ends were covered immediately with wax after cutting, so that any CO<sub>2</sub> ingress or diffusion of moisture takes place only radially. Maximum and minimum depth of carbonation was measured and numerically averaged. During the exposure period, the carbonation penetration depth was periodically measured using the phenolphthalein method by cutting fresh slices from the reference specimen.

At high pH (uncarbonated), the indicator has a bright pink colour. However, below a pH of 8.6 (carbonated condition), it becomes colourless. The interface between the pink and the colourless regions indicates the carbonation front. Maximum and minimum penetration depths were measured and numerically averaged. During the investigation, the carbonation penetration depth was periodically measured. Depths of 2.5, 12 and 15 mm were observed at 15, 30 and 40 days respectively. The low values of carbonation depth observed during the initial days may be attributed to the initial high moisture content in the specimens. Based on the concrete covers described previously (see table 2), it is estimated that the carbonation front reached the rebar after 18, 26 and 39 days for specimens 2, 3 and 4 respectively. The numbers of days has been calculated assuming that carbonation follows a square root time law. The next section correlates these observations (which are made through destructive tests) with ESP obtained non-destructively via the EMI technique.

The baseline signatures of the specimens were first acquired as reference prior to placing in the carbonation chamber. Fig. 3 shows the baseline conductance spectrum of

the PZT patches of three specimens, acquired after 28 days of curing, before being subjected to accelerated carbonation. Even though the initial baseline signatures of the specimens are different, when applying the EMI technique it is the variation of the signature of interest with the baseline signature that is important as it is used here to deduce changes in the specimen.

#### **4. CHANGES IN IMPEDANCE BASED EQUIVALENT PARAMETERS DURING CARBONATION**

Fig. 4 (a, b and c) show the conductance signatures of the bonded PZT patches for the three test specimens (Nos. 2, 3 and 4) acquired during various times. It is worth noting that all the specimens were 28 days old before the initiation of the experiment and hence the majority of the hydration process was already completed. The figures show that the resonance peaks of the conductance signature have changed its magnitude and frequency for all the three specimens with increasing carbonation.

To quantify damage, at first crudely, root mean square deviation (RMSD) metric was utilized, which is defined as [12]

$$RMSD = \sqrt{\frac{\sum_1^N (G_i - G_i^0)^2}{\sum_1^N (G_i^0)^2}} \times 100 \quad (6)$$

where  $G_i$  is the conductance of the PZT patch at any stage during the test and  $G_i^0$  is the baseline value (in pristine condition),  $i$  representing the frequency index (100 to 400 kHz). Fig. 5 (a, b and c) shows the variation of the RMSD index of the three specimens against the exposure period. The RMSD values increased during the exposure period, which provides a useful indicator that the PZT sensors are sensitive enough to identify

changes in the system. This is not always the case, as previous studies on other systems such as reinforced concrete structures and steel bolted joints [6, 12] RMSD sometimes exhibit a random response, hence under these conditions the RMSD approach is unreliable. RMSD is a non parameter based statistical index to quantify the changes in the signature acquired by the PZT patch. Previous studies by the authors (Talakokula et. al. [6]; Bhalla et. al. [12]) have confirmed that it is suitable for preliminary analysis not very reliable for in depth analysis. It just provides the deviation of the raw signature with respect to the baseline, thereby not directly linking to any structure related parameter

#### 4.1 Equivalent stiffness parameters (ESP)

To gain deeper insight into the corrosion mechanism, Equivalent structural parameters were extracted from the impedance spectrum using the computational procedure outlined by Bhalla and Soh [19]. The extracted mechanical impedance  $Z_{s,eff}$  consists of the real and imaginary components  $x$  and  $y$  respectively. Observing the variation of  $x$  and  $y$  closely in the frequency range of 150-250 kHz revealed that the variation is similar to the variation of  $x$  and  $y$  of a parallel spring-damper-mass (k-c-m) combination [20] as shown in Fig. 6 (a). For this system,

$$x = c \quad \text{and} \quad y = m\omega - \frac{k}{\omega} \quad (7)$$

Where  $C$  is the equivalent damping parameter,  $k$  equivalent stiffness parameter (ESP),  $m$  equivalent mass parameter (EMP) and  $\omega$  is the angular frequency. The variation of 'x' and 'y' for both equivalent system (parallel spring-damper-mass) and that of the experimental is shown in Fig. 6 (b and c) for a typical specimen (no.2), confirming the

observation that the host structure has been identified as a parallel spring-damper-mass system.

For this system, the values of the ESP and the EMP of the host structure were determined using Eq. 7 (refer Talakokula et. al [6], for details). Fig. 7 displays the effect of the accelerated carbonation exposure on the identified ESP which shows an initial increase in ESP for all the three specimens. This increase is attributed to calcium carbonate formed during carbonation of the cement phases, filling the pores and leading to an increase in stiffness. However, once the carbonation front reached the steel/concrete interface, a reduction in alkalinity and subsequent break down of the passive film is expected to trigger corrosion. The greater volume of the corrosion products would induce stresses in the adjacent concrete material, leading to the formation of micro-cracks and a decrease in the ESP values. Hence, the phase where the ESP value begins to decrease indicates the initiation of corrosion. From these plots, based on the trend of the ESP, this period can be projected to be lie somewhere between 50 and 90 days of exposure, the exact time of differing from one specimen to other. It should also be emphasised that the ESP values are not directly related to the depth of carbonation. Depths of 2.5, 12 and 15 mm were observed at 15, 30 and 40 days respectively by means of destructive tests conducted on the reference specimen as described before. The carbonation process lowers the local pH around the rebar, allowing corrosion to initiate, which in turn influences the ESP as discussed before. When considered together with the cover depths reported in Table 2, a sequential pattern is noted in relation to the carbonation front, which reached the rebar after 18, 26 and 39 days for specimens 2, 3 and 4 respectively. It can be noted from Fig. 7 that the peak of the ESP plot does indeed occur after these specific periods. The ESP based

diagnosis clearly proves its leverage over the conventional statistical diagnostics such as RMSD as covered before.

In addition, the non-dimensional stiffness loss ( $\Delta k/k$ ) was determined to quantify the level of corrosion damage on account of carbonation. Fig. 8 (a, b and c) shows the variation of ( $\Delta k/k$ ) with the exposure period for the three test specimens. From the figures, it can be observed that for smaller diameter specimen (No. 2), the downward trend of the curve started when the  $\Delta k/k$  value reached 0.45. As the diameter of the specimens increased (Nos. 3 and 4), thereby increasing the cover to steel, it is noted that the peak  $\Delta k/k$  values are lower at 0.4 and 0.3 respectively. Further, relative to the peak value of the ESP, the decrease in the  $\Delta k/k$  values of specimens 2, 3 and 4 are found to be 0.3, 0.2 and 0.28 respectively. Based on the empirical equivalent stiffness model of Talakokula et. al [6], the corrosion process can be identified to be in the “propagation” phase for these values of  $\Delta k/k$ .

#### 4.2. EQUIVALENT MASS PARAMETER (EMP)

The initial mass of all the rebars were measured before embedding them in concrete and after splitting all the specimens, the final mass loss of the steel bars was determined by the gravimetric method after chemically cleaning the corrosion products. The EMP was also calculated directly using Eq. (7) after mathematical calculations (refer Talakokula et. al [6], for details) during the carbonation corrosion exposure, without any destructive measure.

Knowing the actual mass and the PZT identified EMP, a non-dimensional mass model is derived as

$$\left(\frac{\Delta m}{m}\right)_{actual} = \Lambda_m \left(\frac{\Delta m}{m}\right)_{PZT} \quad (8)$$

Where  $\Lambda_m$  is a constant relating PZT identified EMP with actual mass loss determined as 0.54 [6]. This correlation will be useful in calculating the corrosion rates of the rebar non-destructively, because measuring the actual mass loss in real life structures is not possible as rebar is inside the concrete.

#### 4.3. VALIDATION OF NON-DIMENSIONAL MASS MODEL

Knowing the mass loss, the corrosion rate is calculated as described in ASTM G1-03 [32] using the equation

$$\Delta_c = \frac{(k \times \Delta m)}{(a \times T \times D)} \quad (9)$$

where  $\Delta_c$  is the corrosion rate (mm/year)  $K$  is a constant equal to  $8.76 \times 10^4$ ,  $\Delta m$  is the mass loss in g,  $a$  the area in  $\text{cm}^2$ ,  $T$  time of corrosion exposure in hours and  $D$  is the density of steel i.e.  $7.8 \text{ kg/m}^3$ . The corrosion rates were calculated using both actual mass loss as well as the non-dimension mass model Eq. (8) and are tabulated in Table.4. Upon comparing both, it was found that using the model developed, the corrosion rates can be calculated with reasonable accuracy (average error of 10 % only). This is a very important observation, which establishes that the application of the proposed methodology enables circumventing the determination of actual mass loss, which in practice is infeasible.

### 5. CORRELATION WITH MICROSCOPIC IMAGE ANALYSIS AND RAMAN ANALYSIS

To verify the nature of changes highlighted by the ESP, conventionally available experimental techniques including optical microscopy, scanning electron microscopy (SEM) and Raman spectroscopy were applied to representative cross sections of the specimens. The sections were cut during the exposure period for performing these

tests. In order to produce high quality polished sections and reduce the possibility of mechanical damage, the end of each cylinder was embedded in low-viscosity resin at atmospheric pressure prior to polishing. The sections were then cut perpendicularly to the cylinder longitudinal axis (parallel to the basal face) using a diamond impregnated cutting disc in dry conditions. The surface of each section was subsequently ground using progressively finer silicon carbide papers from 180 to 1200 grit size before polishing with 6, 3 and 1  $\mu\text{m}$  diamond paste. A final polish was achieved using colloidal silica suspension. Optical inspection of the polished sections was carried out using a Leica DM ILM inverted metallurgical microscope equipped with an Infinity 1 digital camera (Leica Microsystems, Milton Keynes, United Kingdom). Images of the sections were acquired using Studio Capture Software version 4.0.1.

Figure 9b shows an SEM image taken at 243 days which shows calcium carbonate crystals within the pore structure which can be used to explain the increase in the ESP values on account of stiffening action (see Fig. 9a carbonation penetration phase pre-peak of ESP). It should be noted that calcium carbonate is a stable phase and within the time period between the peak equivalent stiffness at approximately 67 days and the end of the monitoring period when the image was taken at 243 days no significant changes would be expected. Fig. 9c shows cracking in specimen 2, which resulted in the decrease of the ESP values in post-peak phases. It is also noteworthy that such cracking would not be visible in the SEM image presented.

Several cracks (black areas) are visible propagating from the rebar (upper part of the image) towards the external surface (lower part). Cracks often follow the interface between the aggregate and the cement matrix. This results in the decrease of ESP values. The relative ESP values have already indicated the corrosion to be in the propagation phase, which correlates well with the microscopic findings. Hence, the

ESP provides a strong indication of the changes occurring during the carbonation process.

To verify the nature of the oxides formed on the rebar surface (which, through expansion led to the formation of the cracks identified during with the optical microscope), analysis was performed using Raman spectroscopy of the metal phase located at the cement/ rebar interface. A Renishaw inVia Raman Spectrometer with a laser of wavelength 532 nm (green visible light) was used. The laser was set at 100% of the power; and scans were performed between 100 and 3200  $\text{cm}^{-1}$  with only one accumulation and an exposure time of 10 seconds. A WiRE software version 3.4 developed by Renishaw plc, New Mills, Wotton-under-Edge, Gloucestershire, United Kingdom, was used to set the experiment and acquire the spectra.

Fig. 10 shows one of these spectra with the corresponding location along the interface highlighted by a red dot in the box (upper right corner). Peaks in the spectrum are located at 220, 278, 390, 486, 582, 804, 1058, 1280  $\text{cm}^{-1}$ . Data reported in the scientific literature by Oh et. al [30] attributed the peaks at 220, 278 and 1280  $\text{cm}^{-1}$  to hematite  $\alpha\text{-Fe}_2\text{O}_3$ . It is already known, in fact, that depending on the crystallinity and grain size, the characteristic double at 294/225  $\text{cm}^{-1}$  of this mineral in some cases shifts downward in wave number [30]. Peaks at 390, 486 and 582  $\text{cm}^{-1}$  are attributed to goethite  $\alpha\text{-FeOOH}$  [31]. Both these phases are common in the corrosion products associated with rebar corrosion.

## **7. CONCLUSIONS**

This paper has presented a new approach for monitoring the progression of carbonation and the coupled rebar corrosion in RC structures based on the ESP and EMP parameters extracted from the admittance signatures of PZT patches surface-bonded to the rebars.

This is the first ever study involving PZT sensors and utilizing the EMI technique to diagnose carbonation induced corrosion initiation and progression. The main objective was proof-of-concept demonstration of the ESP and EMP based rebar carbonation initiation, progression and quantification. A total of four specimens were tested, all of which showed consistent results, commensurate with the individual cover thickness. The ESP extracted from the admittance signatures of surface-bonded PZT patches is established as a reliable carbonation progression as well as rebar corrosion indicator. ESP correlates well with the microscopic image analysis. The average rate of corrosion has been determined using EMP and compared with the actual corrosion rates using gravimetric mass loss measurements, the error has been found to be 10 % only. The most promising feature of the proposed approach is that the two main phases in the process, namely carbonation penetration through concrete cover and corrosion initiation are determined. The significance of the proposed approach is that it is non-destructive in nature, simple and fully autonomous. The empirical correlation derived from the PZT patches can be utilized in carbonation induced corrosion of rebars in real-life RC structures, where they are not exposed for direct visual check.

## **REFERENCES**

- [1] M. Moreno, W. Morrism, W, M. G. Alvarez and G. S. Duffo, Corrosion of reinforcing steel in simulated concrete pore solutions: Effect of carbonation and chloride content, *Corros Sci*, 42(11) (2004), 2681-2699.
- [2] J. P. Broomfield, J. P, *Corrosion of Steel in Concrete, Understanding, Investigation and Repair*, Second ed., Taylor and Francis, (2007).

- [3] H. A. F. Dehwah, M. Maslehuddin and S. A. Austin, Long-Term Effect Of Sulphate Ions And Associated Cation Type On Chloride Induced Reinforcement Corrosion In Portland Cement Concretes, *Cem. Concr. Compos*, 24 (2002), 17-25.
- [4] P. Claisse, H. Elsayad and E. Ganjian, Permeability and Pore Volume of Carbonated concrete” European concerted action, Final report, Brussels, 1997.
- [5] L. J. Parrott, A review of carbonation in reinforced concrete, British Cement Association, contract report for the Building Research Establishment, C/I-0987, 1987.
- [6] V. Talakokula, S. Bhalla and A. Gupta, (2014) “Corrosion Assessment of Reinforced Concrete Structures Based on Equivalent Parameters Using Electro-Mechanical Impedance Technique”, *J Intel Mat Syst Str*, Volume 25 (4), pp 484-500.
- [7] G. Miller, P. Gaydecki, S. Quek, B. Fernandes and M. Zaid, A combined Q and heterodyne sensor incorporating real-time DSP for reinforcement imaging, corrosion detection and material characterisation, *Sensor Actuat A-Phys*, 121 (2) (2005), 339-346.
- [8] T. Ikeda, *Fundamentals of Piezoelectricity*, Oxford University Press, Oxford 1990.
- [9] W. Li, Y. Cho, Quantification and imaging of corrosion wall thinning using shear horizontal guided waves generated by magnetostrictive sensors, *Sensor Actuat A-Phys*, 232 (2015), 251-258.
- [10] C. K. Soh, K. K. H. Tseng, S. Bhalla, S. and A. Gupta, Performance of Smart Piezoceramic Patches in Health Monitoring of a RC Bridge, *Smart Mater. Struct.*, 9(4) (2000), 533-542.

- [11] C. K. Soh and S. Bhalla, Calibration of Piezo-impedance Transducers for Strength Prediction and Damage Assessment of Concrete, *Smart Mater. Struct.*, 14 (2005), 671-684.
- [12] S. Bhalla, A. P. R. Vittal, and M. Veljkovic, Piezo-Impedance Transducers for residual Fatigue Life Assessment of Bolted Steel Joints, *Struct. Health Monit.*, 11(6) (2012), 733-750.
- [13] D. M. Pears, G. Park and D. J. Inman, Improving accessibility of the Impedance-Based Structural Health Monitoring Method, *J Intel Mat Syst Str*, 15 (2) (2004), 129-139.
- [14] T. G. Overly, G. Park, K. M. Farinholt and C. R. Farrar, Development of an extremely compact impedance-based wireless sensing device”, *Smart Mater. Struct*, 17(6) (2008), 065011.
- [15] S. Bhalla, A. Gupta, S. Bansal, S. and A. Garg, A , Ultra Low Cost Adaptation of Electro-mechanical Impedance for Structural health Monitoring”, *J Intel Mat Syst Str*, 20 (2009), 991-999.
- [16] V. Giurgiutiu and A. N. Zagrai, Embedded Self-Sensing Piezoelectric Active Sensors for On-Line Structural Identification, *J Vib Acoust, ASME*, 124 (2002), 116-125.
- [17] C. Liang, F. P. Sun and C. A. Rogers, Coupled Electro-Mechanical Analysis of Adaptive Material Systems- Determination of the Actuator Power Consumption and System Energy Transfer”, *J Intel Mat Syst Str*, 5 (1994), 12-20.
- [18] S. Bhalla and C. K. Soh, Structural Health Monitoring by Piezo-Impedance Transducer: Modelling, *J. Aerospace Eng, ASCE*, 17(4) (2004a), 154-165.
- [19] S. Bhalla, C. K. Soh, C. K, Structural Health Monitoring by Piezo-Impedance Transducer: Application, *J. Aerospace Eng, ASCE*, 17(4) (2004b),, 166-171.

- [20] E. L. Hixon, Mechanical Impedance Shock and Vibration Handbook, edited by C. M. Harris, 3rd edition, Mc Graw Hill Book Co, New York, 1988.
- [21] IS 456, Indian Standard plain and reinforced concrete, code of practice. Bureau of Indian Standards, New Delhi, India, 2000.
- [22] IS 1786, Indian Standard Specification for High Strength Deformed Steel Bars and Wires for Concrete Reinforcement, Bureau of Indian Standards, New Delhi, 1985.
- [23] PI Ceramic, Product information catalogue”, Lindenstrabe, Germany, [www.piceramic.de](http://www.piceramic.de), 2012.
- [24] IS 383, Indian Standard specification for coarse and fine aggregates from natural sources for concrete, Bureau of Indian Standards, New Delhi, India, 1970.
- [25] Agilent Technologies, Test and measurement catalogue, (2011), [www.agilent.com](http://www.agilent.com).
- [26] Jana, D. and Erlin, B., “Carbonation as an Indicator of Crack Age”, ACI Concrete International, May 2007, pp. 61-64.
- [27] IS: 10262-2009 Indian Standard Specification for Concrete Mix Proportions: Guidelines, Bureau of Indian Standards, New Delhi, 2009.
- [28] C. L. Page, Basic Principles of Corrosion” Schiessl P. (editor), Corrosion of steel in concrete, Chapman and Hall, London, 1988.
- [29] M. L. Castellote, C. Fernandez, C. Andrade and Alonso, Chemical changes and phase analysis of OPC pastes carbonated at different CO<sub>2</sub> concentrations. Mater. Struct., 42 (2009), 515-525.
- [30] S. J. Oh, D. C. Cook and H. E. Townsend, Characterization of Iron Oxides Commonly Formed as Corrosion Products on Steel, Hyperfine Interact, 112 (1998), 59-66

[31] A. Wang, L. A. Haskin and B. L. Jolliff, B.L, Characterization of Mineral Products of Oxidation and Hydration by Laser Raman Spectroscopy - Implications for In Situ Petrologic Investigation on the Surface of Mars, in: Lunar and Planetary Institute Science Conference Abstracts, 29 (1998), 1819.

[32] ASTM G I -03. Standard Practice for Preparing, Cleaning and Evaluating Corrosion Test Specimens, (2003). West Conshohocken, PA

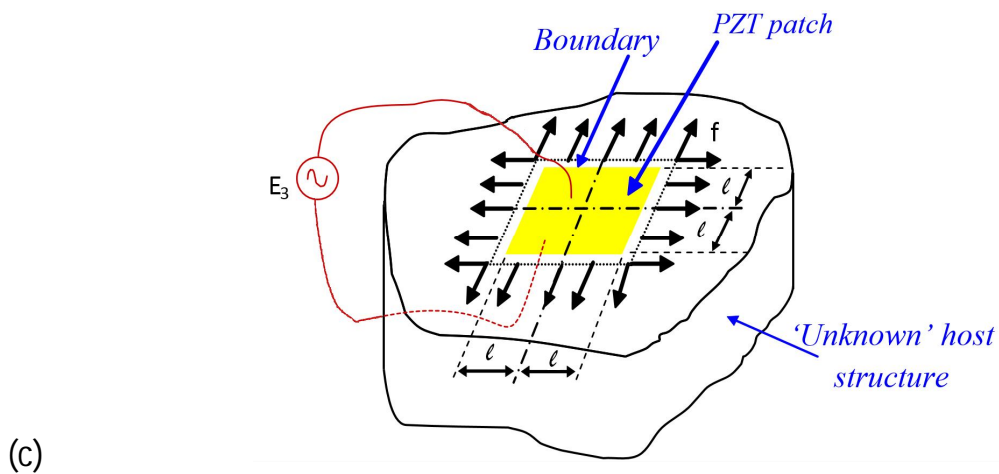
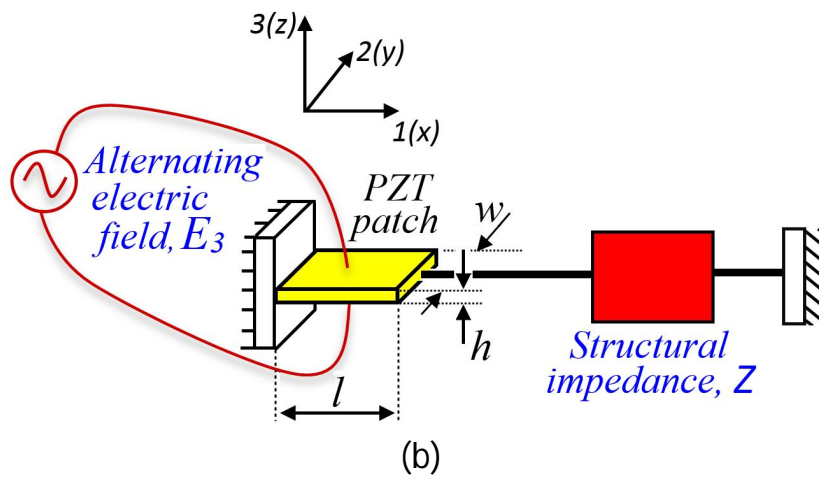
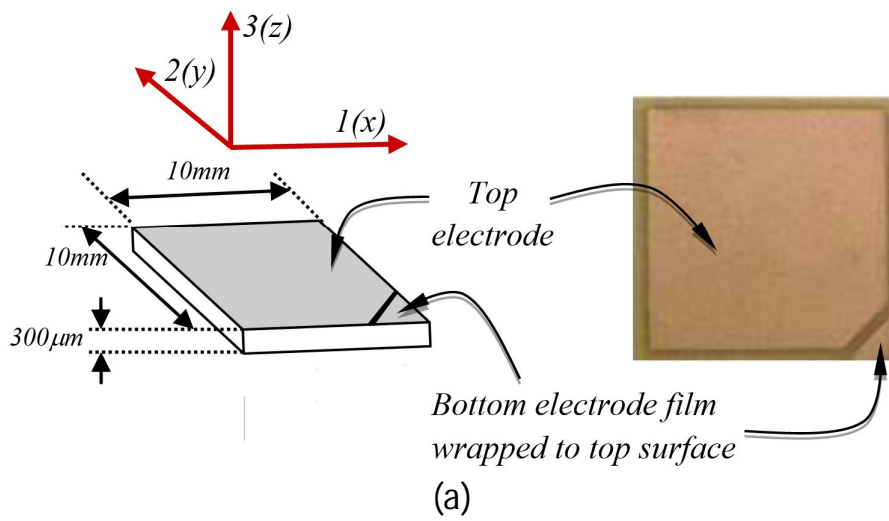
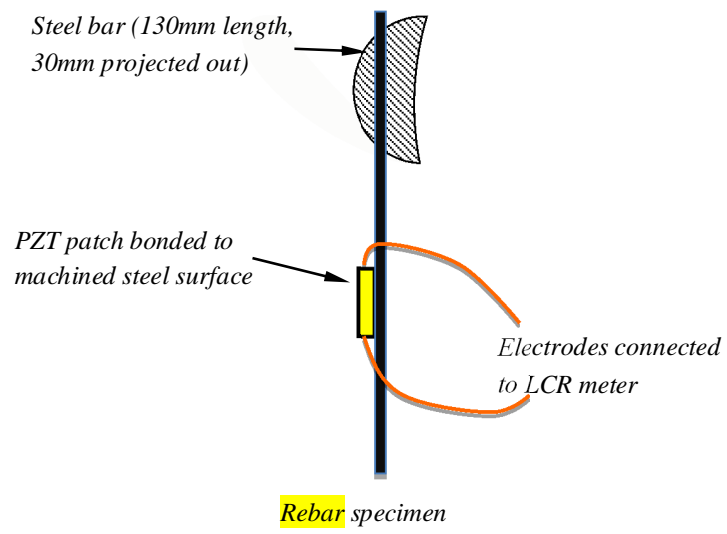


**Figure 1** PZT patch and its interaction with host structure.

(a) Geometric details of a typical PZT patch (b) Modelling scheme of PZT-structure interaction 1D (c) A PZT patch bonded to the host structure 2D



(a)



(b)

**Figure 2** Rebar specimen  
(a) Typical specimen geometry (b) typical sample

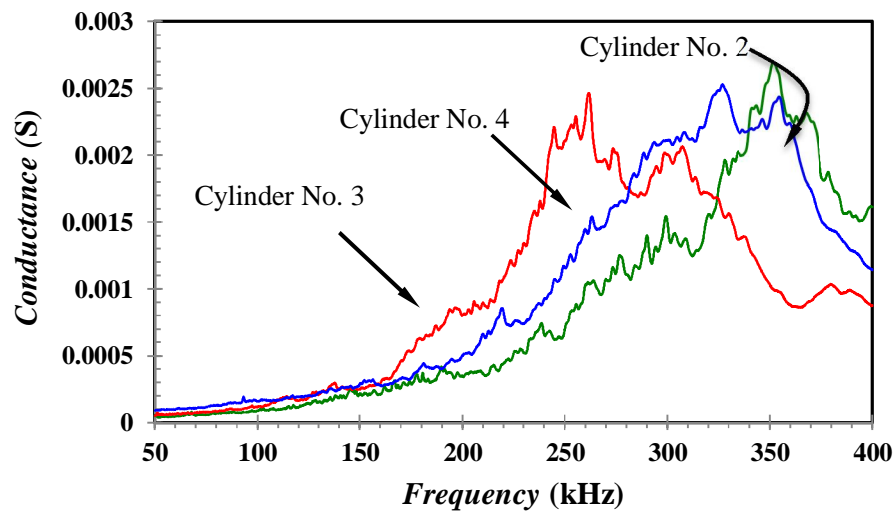


**Figure 3** Baseline conductance signatures of PZT patch embedded in RC cylindrical specimens

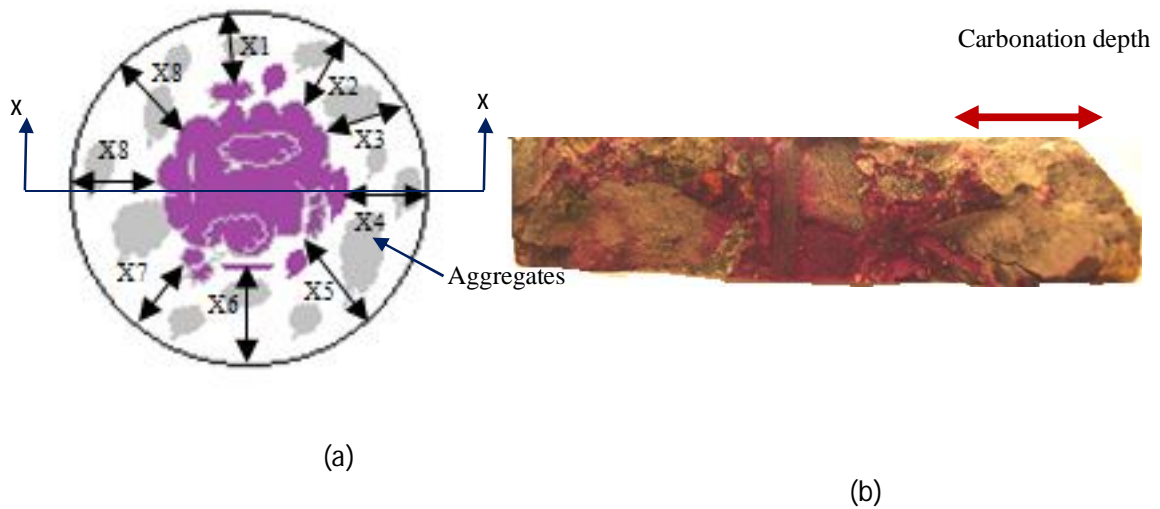
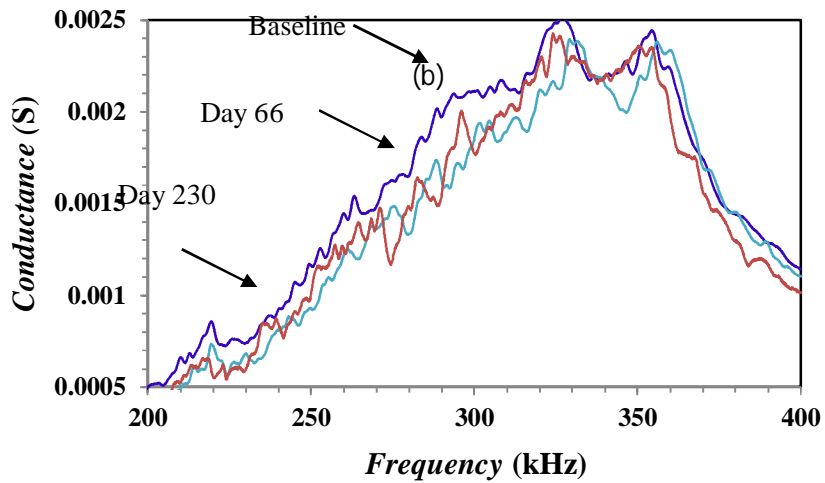
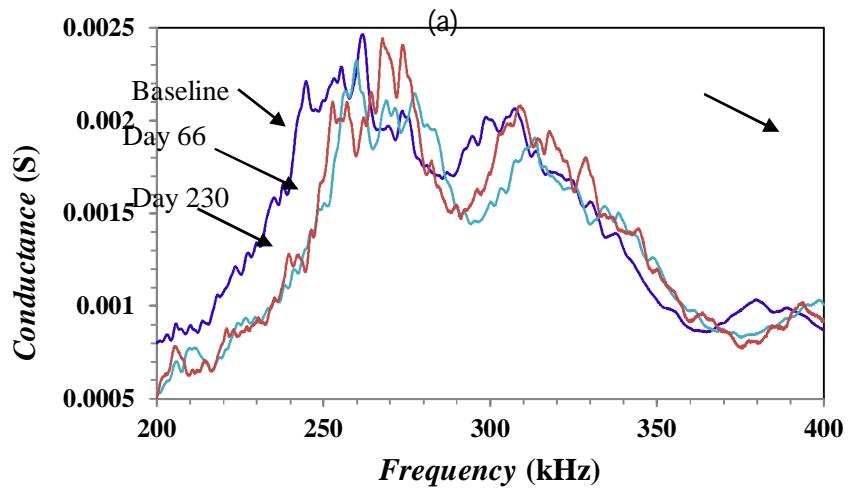
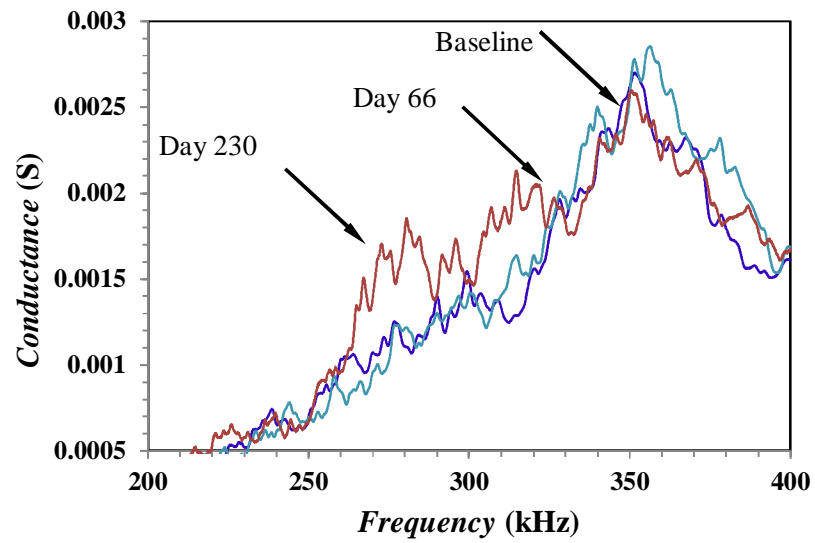
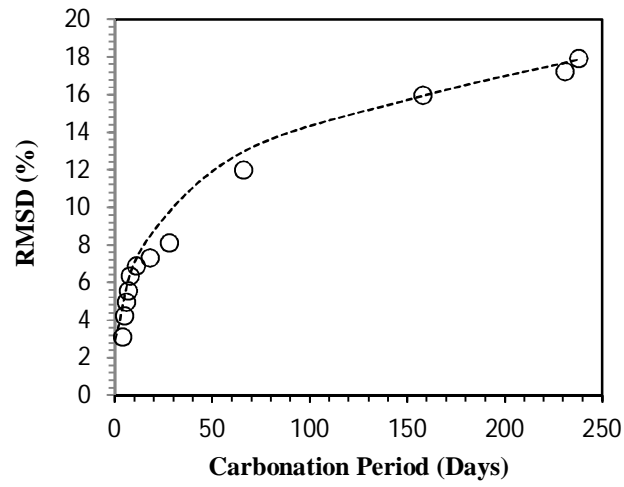


**Figure 4** Phenolphthalein indicator solution applied to a fresh fracture slice of concrete  
 (a) Schematic diagram showing reading locations  
 (b) Section xx

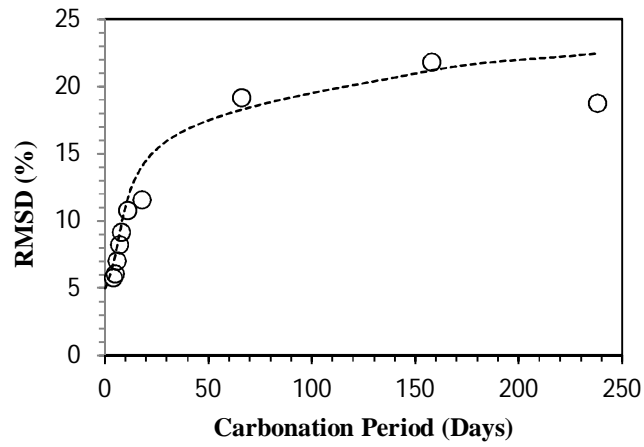


(c)

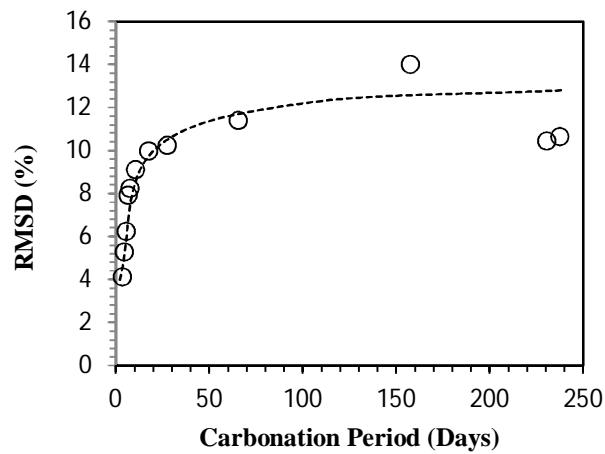
**Figure 5** Variation of conductance signatures during accelerated carbonation corrosion process  
 (a) Cylinder No. 2 (b) Cylinder No. 3 (c) Cylinder No. 4



(a)



(b)



(c)

**Figure 6** Variation of Variation of RMSD index during accelerated carbonation corrosion process  
 (a) Cylinder No. 2 (b) Cylinder No. 3 (c) Cylinder No. 4

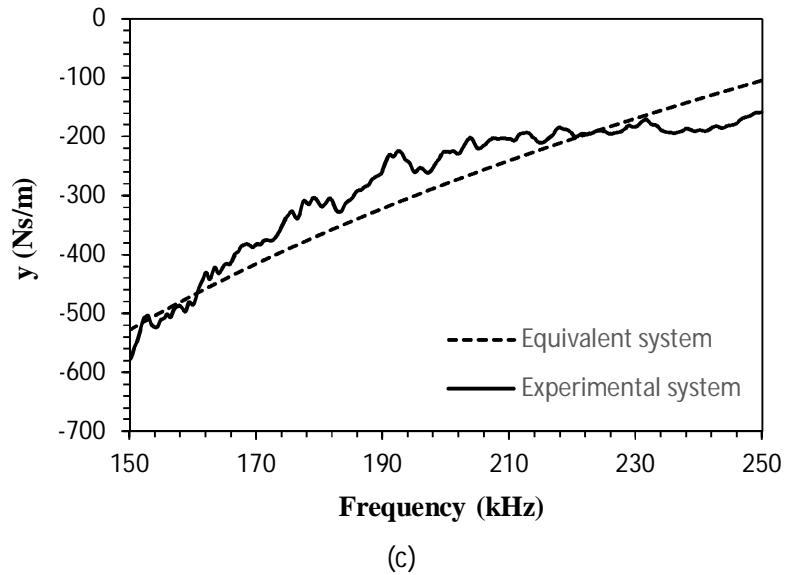
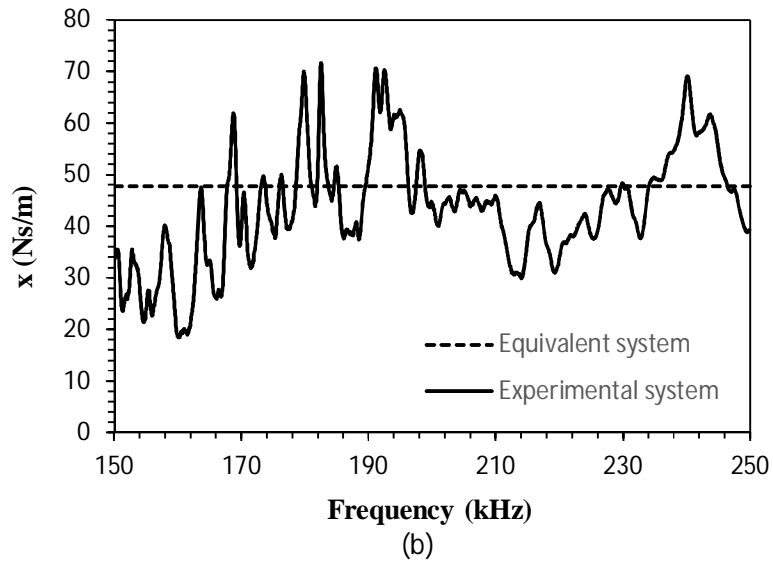
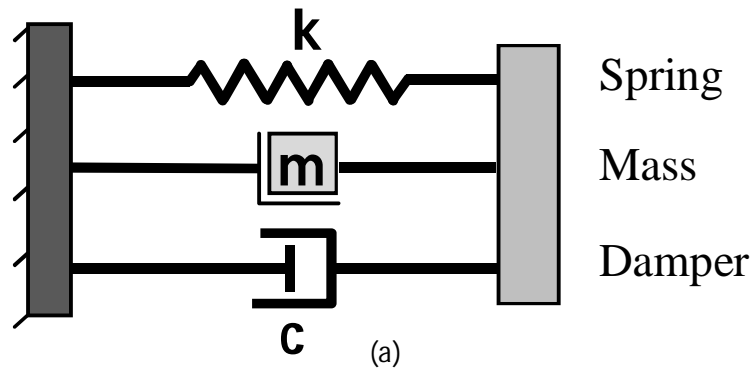
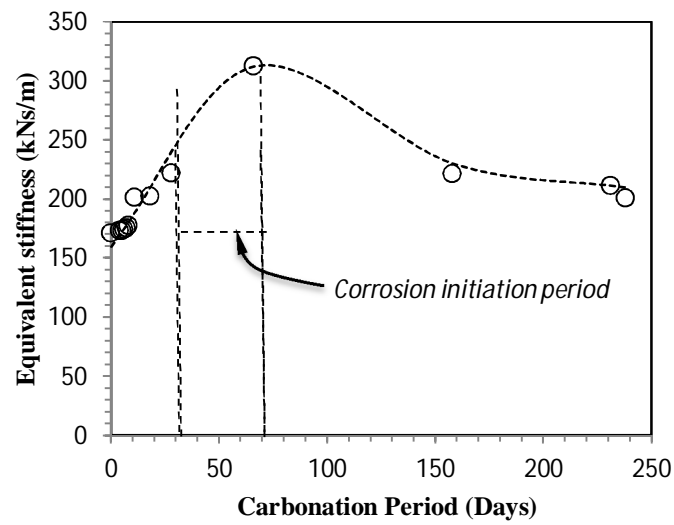
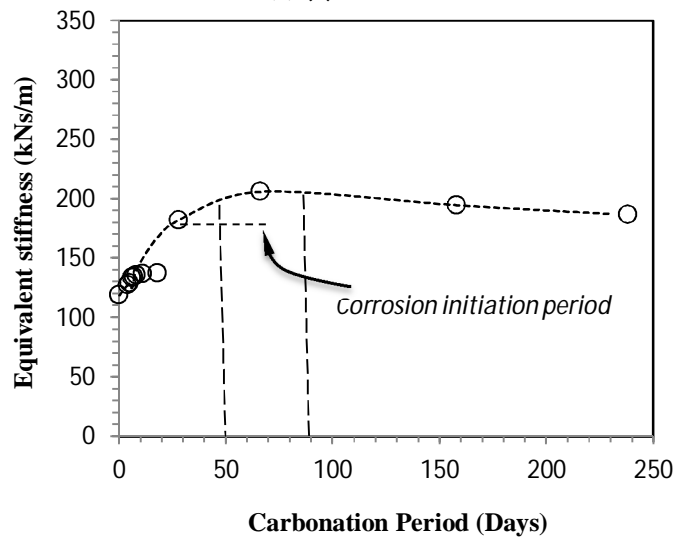


**Figure 7** Equivalent stiffness parameters.

(a) Identified Parallel combination of spring-mass-damper system (b) Comparison of experimental plots of  $x$  with those of identified system for typical cylinder (No. 2) (c) Comparison of experimental plots of  $y$  with those of identified system for typical cylinder (No. 2)



(c) (a)



(b)

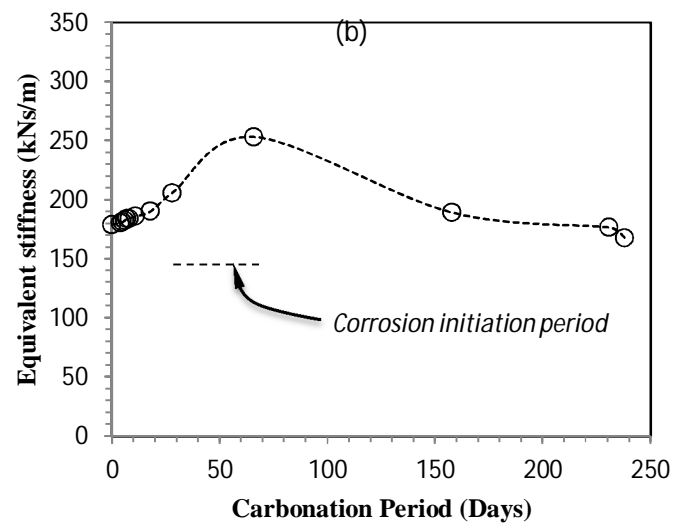
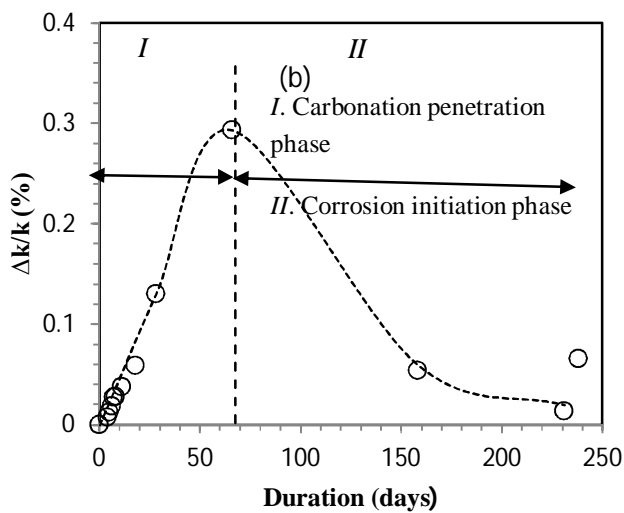
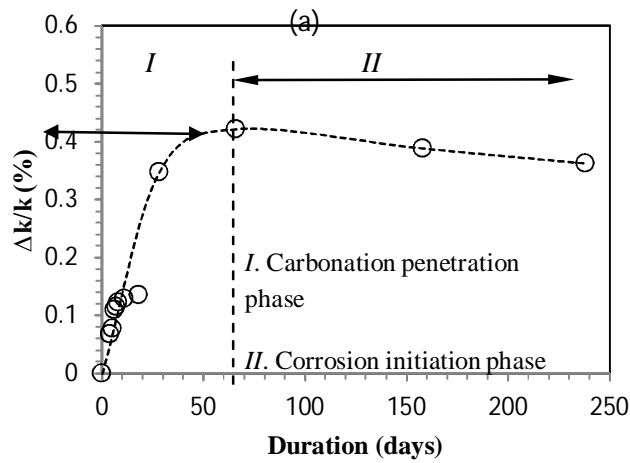
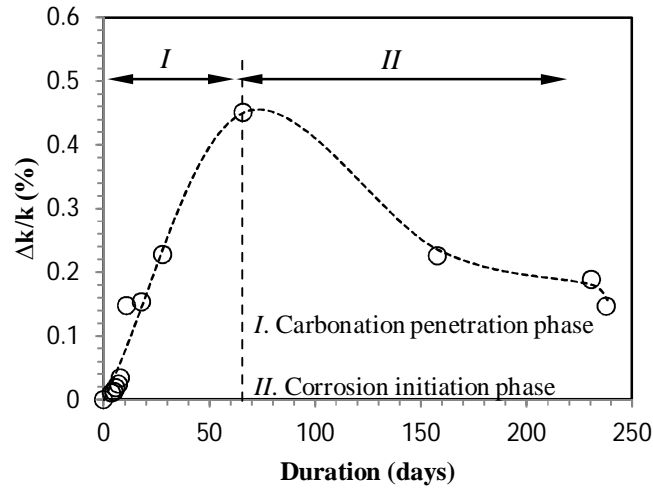
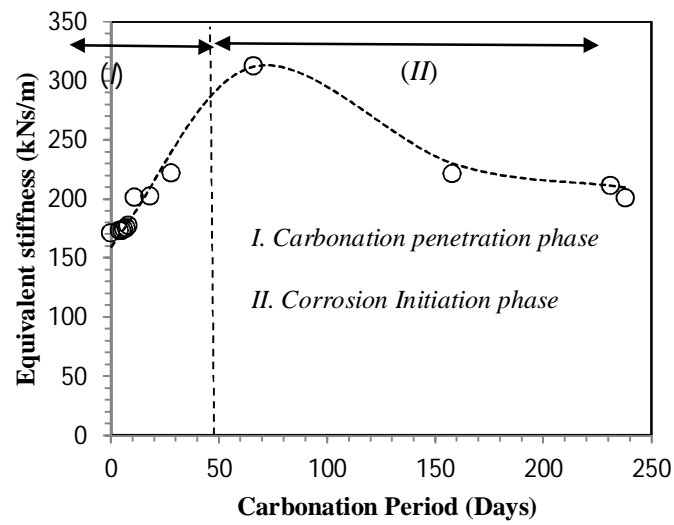


**Figure 8** Variation of equivalent stiffness during accelerated carbonation corrosion process  
 (a) Cylinder No. 2 (b) Cylinder No. 3 (c) Cylinder No. 4

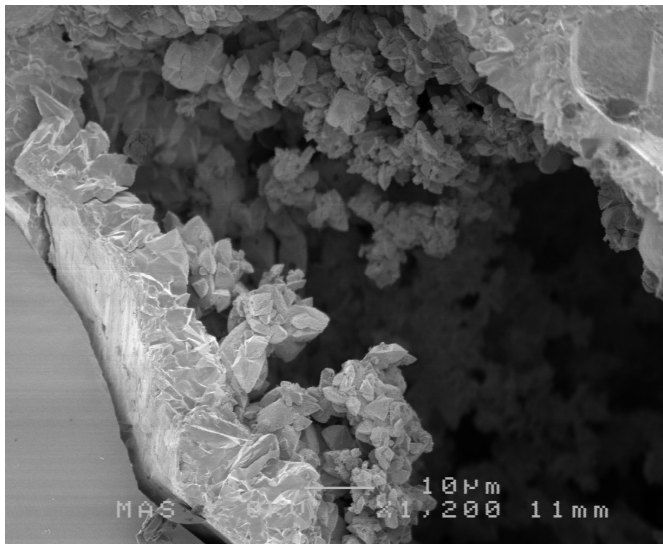


(27)

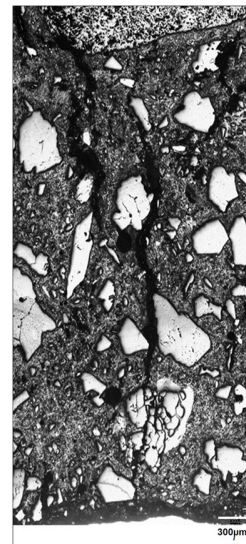
**Figure 9** Variation of  $\Delta k/k$  during accelerated corrosion process  
 (a) Cylinder No. 2 (b) Cylinder No. 3 (c) Cylinder No. 4



(a)



(b)



(c)

**Figure 10** Correlation of ESP values with SEM and optical images. (a) ESP values for carbon penetration phase (Region I) and corrosion initiation/cracking phase (Region II). (b) high magnification secondary electron image (scale bar 10µm) corresponding to a typical internal crack microstructure at 243 days (c) low magnification optical image (scale bar 300µm) of a polished section between the rebar (top) and sample edge (bottom) at 243 days.

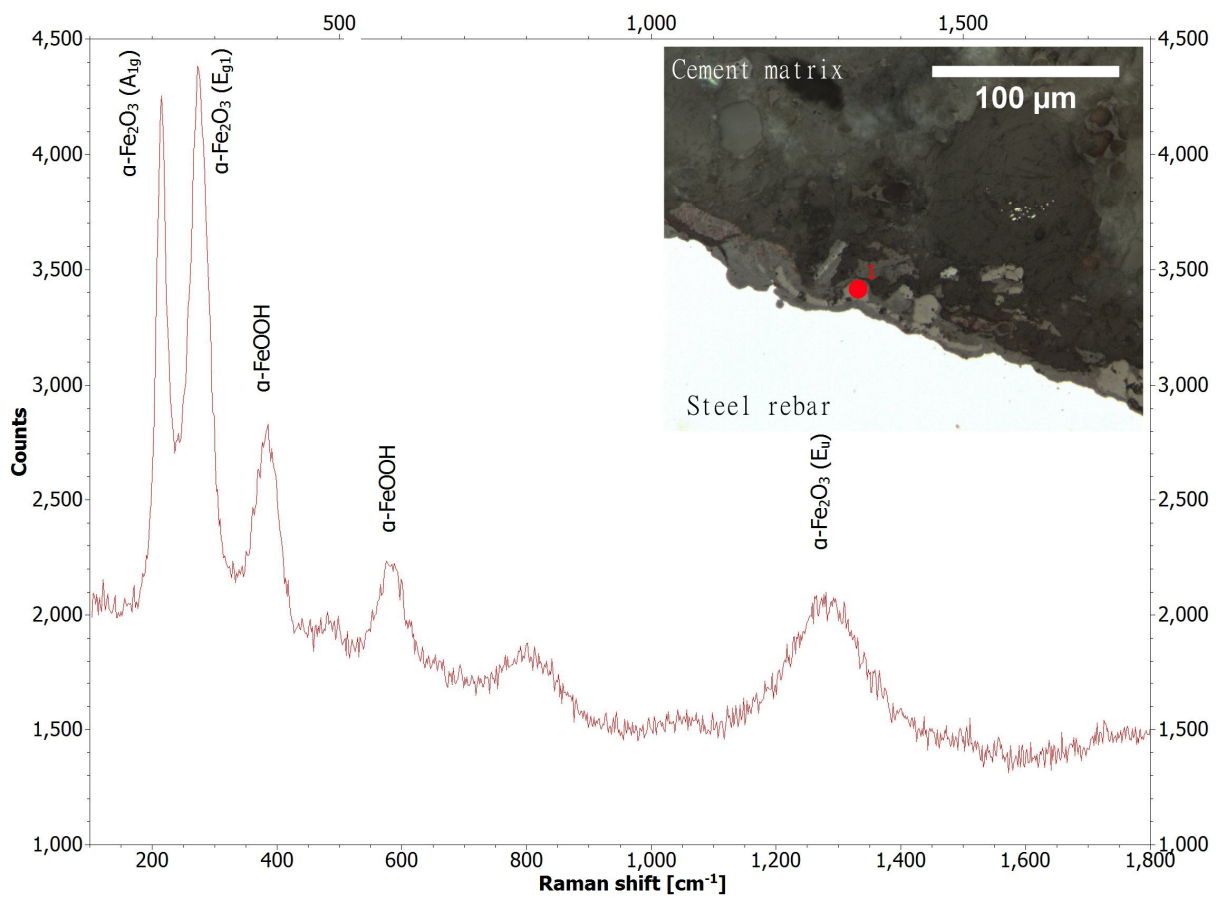


**Figure 11** Raman spectrum of  $\alpha$ -hematite ( $\text{Fe}_2\text{O}_3$ ) oxide layer on steel rebar extracted from sample 2 at 243 days. Inset shows optical image of polished section and location of analysis. Cement matrix shown in top right hand side dark area and steel re bar shown in light bottom left hand side.

**Table 1.** Comparison of various corrosion detection techniques [6]

<b>Detection technique</b>	<b>Advantage</b>	<b>Disadvantage</b>
<b>Half-cell potential measurements</b>	<ul style="list-style-type: none"> <li>• Common procedure for routine inspection of RC structures</li> <li>• Simple and cost-effective</li> </ul>	<ul style="list-style-type: none"> <li>• Provides only information on probability of corrosion, cannot indicate corrosion rates.</li> <li>• Values can be misleading</li> <li>• Only a first approach to corrosion detection and must be complimented by other techniques for corrosion rates</li> <li>• Requires the knowledge of potential in non-corroded areas</li> </ul>
<b>Polarization resistance technique</b>	<ul style="list-style-type: none"> <li>• Provides a measurement of the corrosion rate</li> <li>• An instantaneous measuring system.</li> </ul>	<ul style="list-style-type: none"> <li>• In most cases, e.g., when the cover concrete is too thick, the confinement of the polarization area may not be achieved.</li> </ul>
<b>Gravimetric mass loss measurements</b>	<ul style="list-style-type: none"> <li>• Most effective method for calculating corrosion rates</li> </ul>	<ul style="list-style-type: none"> <li>• Destructive method</li> <li>• Requires the knowledge of the mass of rebar in healthy state</li> </ul>
<b>EMI technique</b>	<ul style="list-style-type: none"> <li>• The assessment is Non-destructive in nature</li> <li>• Detection is based on the structural response.</li> <li>• Equivalent structural parameters can be extracted thus circumventing the determination of actual parameters</li> <li>• Reduces required sensors by allowing self-sensing actuation</li> <li>• Sensitive and changes to damage induced due to carbonation corrosion</li> </ul>	<ul style="list-style-type: none"> <li>• Maintaining sensor health and bonding is important.</li> <li>• Requires knowledge of a healthy structure.</li> </ul>

**Table 2.** Specimen identification number, dimensions and cover to reinforcement

Specimen	Specimen size (mm)	Cover to reinforcement (mm)
1	60 x 100 (Reference specimen)	22
2	25 x 100	4.5
3	35 x 100	9.5
4	45 x 100	14.5

**Table 3.** Concrete mix design specification

Materials	Quantity
Water cement ratio	0.4
OPC (kg/m <sup>3</sup> )	500
Fine aggregate (kg/m <sup>3</sup> )	570.5
Coarse aggregate (kg/m <sup>3</sup> ) 10mm	1062.2
Slump (mm)	100

**Table 4** Comparison of corrosion rates for specimens Nos. 2, 3 and 4 determined from gravimetric mass loss and PZT identified mass loss.

Specimen	Actual corrosion rates using gravimetric mass loss (mm/year)	Corrosion rates using PZT identified mass loss after incorporating $\Lambda_m$ (mm/year)	Percentage error
2	0.059	0.067	13.5
3	0.048	0.052	8.3
4	0.012	0.013	8.3